Design and flight testing of incremental nonlinear dynamic inversion based control laws for a passenger aircraft

Grondman, Fabian; Looye, Gertjan H.N.; Kuchar, Richard O.; Chu, Q. Ping; van Kampen, Erik Jan

DOI
10.2514/6.2018-0385

Publication date
2018

Document Version
Accepted author manuscript

Published in
AIAA Guidance, Navigation, and Control

Design and Flight Testing of Incremental Nonlinear Dynamic Inversion based Control Laws for a Passenger Aircraft

F. Grondman,* G.H.N. Looye,† R. Kuchar,‡ Q.P. Chu§ and E. van Kampen¶

German Aerospace Center DLR, Münchener Straße 20, 82234 Weßling, Germany

Delft University of Technology, P.O. Box 5058, 2626HS Delft, The Netherlands

This paper describes the design, implementation and flight testing of flight control laws based on Incremental Nonlinear Dynamic Inversion (INDI). The method compares commanded and measured accelerations to compute increments on the current control deflections. This results in highly robust control solutions with respect to model uncertainties as well as changes in aircraft dynamic characteristics of failure cases during flight. At the same time, the complexity of the algorithms is similar to classical ones. The key for practical implementation is in ensuring synchronization between angular acceleration and control deflection measurements or estimates. The underlying theory and practical design methods of INDI are very well understood, but implementation and testing has remained limited to sub-scale UAVs. The main contribution of this paper is to present the design and validation of manual attitude control functions for a Cessna Citation II experimental aircraft, covering control structure design, application of INDI, design optimization, robustness analyses, software implementation, ground and flight testing. For comparison, also control laws based on classical Nonlinear Dynamic Inversion were implemented and flown. The flight tests were highly successful and marked the first successful demonstration of INDI on a CS-25 certified aircraft. The flight test results proved that INDI clearly outperforms NDI and provided valuable lessons-learnt for future applications.

Nomenclature

A_x, A_y, A_z	Specific forces along body X/Y/Z axis, g
C	Dimensionless coefficient
$\boldsymbol{F}$	Force, N
$\boldsymbol{J}$	Inertia matrix, kg·m^2
J	Moment of Inertia, kg·m^2
K	Gain
$\boldsymbol{M}$	Moment, Nm
M	Mach number
$N1$	Fan speed, s^{-1}
S	Wing surface area, m^2
$\boldsymbol{V}$	Velocity vector, m/s
V	Airspeed, m/s
a_x, a_y, a_z	Linear accelerations along body X/Y/Z axis, m/s^2
b	Wing span, m^2
$\bar{c}$	Mean aerodynamic chord, m

*Graduate student, Faculty of Aerospace Engineering, Control and Simulation Division, Delft University of Technology

†Head, Department of Aircraft Systems Dynamics, Institute of System Dynamics and Control, German Aerospace Institute

‡Research associate, Department of Aircraft Systems Dynamics, Institute of System Dynamics and Control, German Aerospace Institute

§Associate Professor, Faculty of Aerospace Engineering, Control and Simulation Division, Delft University of Technology

¶Assistant Professor, Faculty of Aerospace Engineering, Control and Simulation Division, Delft University of Technology

g	Gravity constant, m/s^2
h	Altitude, m
m	Mass, kg
$\boldsymbol{p}$	Model parameters
p, q, r	Roll, pitch and yaw rate around the body X/Y/Z axis, rad/s
$\boldsymbol{r}$	Position vector, m
t	Time, s
$\boldsymbol{u}$	Input vector
u, v, w	Velocity components along body X/Y/Z axis, m/s
$\boldsymbol{x}$	State vector
$\boldsymbol{y}$	Output vector
Symbol	
α, β, γ	Angle of attack, angle of sideslip and flight path angle, rad
$\boldsymbol{\delta}$	Control surface deflection vector, rad
δ	Control surface deflection scalar, rad
ζ	Damping ratio
ϕ, θ, ψ	Roll, pitch and yaw angle, rad
$\boldsymbol{\nu}$	Virtual control vector
ν	Virtual control scalar
ρ	Air density, kg/m^3
τ	Time constant, time delay, s
$\boldsymbol{\omega}$	Angular rate vector, rad/s
ω	Frequency, rad/s
Subscript	
0	Current point in time
A	Aerodynamic
D, Y, L	Force along the stability X/Y/Z axis, N
E	Earth
I	Integrator
T	Thrust
a	Airframe, air-mass
a, e, r	Aileron, elevator, rudder
act	Actuator
b	Body
c	Control effectors
est	Estimate
fbw	Fly-By-Wire
fil	Filter
h	Hedge
i	Inertial
l, m, n	Moment around the body X/Y/Z axis, Nm
min, max	Minimum, maximum
o	Other
plt, com, ref	Pilot, command, reference
s	Stability
$sync$	Synchronization
tas, cas	True airspeed, calibrated airspeed
tc	Turn compensation
Superscript	
b	Body
cg	Center of gravity
s	Stability

I. Introduction

Current fight control techniques are most often based on classical control. In recent years, however, modern methods such as Nonlinear Dynamic Inversion (NDI) find more and more applications[1,2]

Modern Fly-By-Wire (FBW) flight control systems provide augmented stability and control in nominal conditions. In case of severe or unforeseen failures or changes in aircraft behaviour (e.g. due to icing), the control system will howhever revert back to reversionary modes or even direct control.[3] This implies that the control law functionality is partly reduced or abandoned. This behaviour is undesirable as the pilot work load is not only increased due to failure, but also due to aircraft control. Developments subsequently focus on maintaining functionality, even in case of such failures. Research in this field includes reliable fault detection and diagnosis, and control reconfiguration.[3,4] One aspect is the adaptation of flight control laws to unforeseen circumstances and failures.

NDI is an attractive control strategy for adaptation as it globally linearises the system dynamics and decouples the control axes.[5] Moreover, it is clear which parameters and parts require adaptation in case of changed aircraft behaviour. However, extension to fault tolerance requires failures and model changes to be completely identified online.[6]

Incremental Nonlinear Dynamic Inversion (INDI) retains the advantages of NDI but attempts to solve the identification problem by reduced model-dependency. By feeding back synchronous measurement or estimation of control deflection and angular acceleration, the required model knowledge is reduced to the control effectiveness. Implementation was initially considered problematic, but due to synchronization, the control laws run reliably at sample times as in current control computers.

The method first appeared in literature as simplified Nonlinear Dynamic Inversion[7–9] before being formalized as Incremental Nonlinear Dynamic Inversion by Sierbling et al.[10] INDI has found several applications ranging from fixed-wing aircraft and spacecraft[10,11] to helicopters and quadcopters.[12–14]

A first succesful demonstration of INDI was performed by the German Aerospace Center (DLR) in cooperation with Delft University of Technology (TU Delft) at the University of Minnesota.[15] Control laws based on INDI were implemented and tested on the FASER, a sub-scale fixed-wing UAV. Recently, DLR and TU Delft also flight tested an Incremental Backstepping (IBS) variant on this platform.[16] INDI has been succesfully implemented and tested on a quadcopter as well.[14] Due to the promising results obtained on sub-scale UAVs, the next logical step is to demonstrate INDI on a CS-25 certified aircraft.

The main contribution of this paper is to present the design and validation of manual attitude control functions for a Cessna Citation II experimental aircraft, covering control structure design, application of INDI, design optimization, robustness analyses, software implementation, ground and flight testing. For comparison, also control laws based on classical NDI are implemented and flown. The Cessna Citation II PH-LAB is a modified business jet operated by the faculty of Aerospace Engineering of TU Delft. With its newly certified Fly-By-Wire system,[17] the PH-LAB is a highly promising platform for testing advanced flight control laws.

The manual flight control functions presented in this paper combine Rate Control Attitude Hold (RCAH) and Attitude Control (AC) for pitch and roll with sideslip augmentation.[18] An additional feature is Pseudo Control Hedging (PCH),[19] used for adaptation of the reference model output in case of actuator saturation. Note that these control laws build upon earlier research conducted by DLR. Over the years, DLR has done flight experiments with various control laws based on classical NDI.[18,20–22] These experiments were conducted using the now-retired VFW-16 ATTAS testbed.

The outline of this paper is as follows. In Section II, the theory of NDI, INDI and PCH will be briefly reviewed. Thereafter, Section III discusses the PH-LAB research aircraft and corresponding model used for the analysis and synthesis of the control laws. The control law design is presented in Section IV, including inner and outer loop, signal processing algorithms and parameter optimization. The resulting control design is validated in Section V, presenting the simulator assessment and clearance, rig testing and flight tests. Finally, the paper is concluded in Section VI.

II. Incremental Nonlinear Dynamic Inversion

A. Nonlinear Dynamic Inversion

The general idea of NDI is to compensate the nonlinear system dynamics by means of feedback of the inverse model equations such that the closed loop system appears in a linear form. The desired closed loop response can then be imposed via conventional linear controllers.[5]

It is assumed that the model of the nonlinear system has the following control-affine form:

$$\dot{\boldsymbol{x}} = \boldsymbol{f}(\boldsymbol{x}, \boldsymbol{p}) + \boldsymbol{G}(\boldsymbol{x}, \boldsymbol{p})\boldsymbol{u} \tag{1}$$

$$\boldsymbol{y} = \boldsymbol{h}(\boldsymbol{x}, \boldsymbol{p}) \tag{2}$$

$$\boldsymbol{y}_o = \boldsymbol{h}_o(\boldsymbol{x}, \boldsymbol{p}) \tag{3}$$

Where $\boldsymbol{x} \in \mathbb{R}^n$ is the state vector, $\boldsymbol{u} \in \mathbb{R}^m$ the input vector containing only inputs that may be used by the controller, $\boldsymbol{y} \in \mathbb{R}^m$ the output vector containing the outputs to be controlled (i.e. control variables), $\boldsymbol{y}_o$ contains any other outputs of the system, $\boldsymbol{f}$, $\boldsymbol{h}$ and $\boldsymbol{h}_o$ are smooth vector fields, $\boldsymbol{G} \in \mathbb{R}^{n \times m}$ is a matrix with columns of smooth vector fields and $\boldsymbol{p}$ contains the model parameters.

Differentiation of the output equation $\boldsymbol{h}$ results in:

$$\dot{\boldsymbol{y}} = \frac{\partial \boldsymbol{h}(\boldsymbol{x}, \boldsymbol{p})}{\partial \boldsymbol{x}} \frac{\mathrm{d}\boldsymbol{x}}{\mathrm{d}t} = \nabla \boldsymbol{h}(\boldsymbol{x}, \boldsymbol{p})\big(\boldsymbol{f}(\boldsymbol{x}, \boldsymbol{p}) + \boldsymbol{G}(\boldsymbol{x}, \boldsymbol{p})\boldsymbol{u}\big) = L_{\boldsymbol{f}}\boldsymbol{h}(\boldsymbol{x}, \boldsymbol{p}) + L_{\boldsymbol{G}}\boldsymbol{h}(\boldsymbol{x}, \boldsymbol{p})\boldsymbol{u} \tag{4}$$

Where $L_{\boldsymbol{f}}\boldsymbol{h}$ and $L_{\boldsymbol{G}}\boldsymbol{h}$ are the first-order Lie derivatives along $\boldsymbol{f}$ and $\boldsymbol{G}$, respectively. It is assumed that $L_{\boldsymbol{G}}\boldsymbol{h}$ is non-singular and that each output has an order of 1 relative to at minimum one of the inputs (i.e. $L_{\boldsymbol{G}}\boldsymbol{h} \neq 0$). In this case NDI can be applied to Equation (4).[5] Defining the virtual control input as $\boldsymbol{\nu} = \dot{\boldsymbol{y}}$ and inverting Equation (4), the following control law is obtained:

$$\boldsymbol{u} = \big(L_{\boldsymbol{G}}\boldsymbol{h}(\hat{\boldsymbol{x}}, \boldsymbol{p}^*)\big)^{-1}\big(\boldsymbol{\nu} - L_{\boldsymbol{f}}\boldsymbol{h}(\hat{\boldsymbol{x}}, \boldsymbol{p}^*)\big) \tag{5}$$

The vectors $\hat{\boldsymbol{x}}$ and $\boldsymbol{p}^*$ contain the computed or estimated states from $\boldsymbol{y}$ and $\boldsymbol{y}_o$, and the assumed values for the model parameters, respectively. Substituting the control law (Equation (5)) into Equation (4):

$$\dot{\boldsymbol{y}} = L_{\boldsymbol{f}}\boldsymbol{h}(\boldsymbol{x}, \boldsymbol{p}) + L_{\boldsymbol{G}}\boldsymbol{h}(\boldsymbol{x}, \boldsymbol{p})\Big(\big(L_{\boldsymbol{G}}\boldsymbol{h}(\hat{\boldsymbol{x}}, \boldsymbol{p}^*)\big)^{-1}\big(\boldsymbol{\nu} - L_{\boldsymbol{f}}\boldsymbol{h}(\hat{\boldsymbol{x}}, \boldsymbol{p}^*)\big)\Big) \tag{6}$$

When $\boldsymbol{x}$ and $\boldsymbol{p}$ are exactly known ($\hat{\boldsymbol{x}} = \boldsymbol{x}$ and $\boldsymbol{p}^* = \boldsymbol{p}$), Equation (6) reduces to:

$$\dot{\boldsymbol{y}} = \boldsymbol{\nu} \quad \Leftrightarrow \quad \boldsymbol{y}(t) = \int_0^t \boldsymbol{\nu}(\tau)\mathrm{d}\tau \tag{7}$$

The resulting control law linearises the system dynamics, reducing the input-output response to a set of integrators. Note that for stability, the relation between $\boldsymbol{y}$ and $\boldsymbol{u}$ has to be minimum phase.[5]

B. Incremental Nonlinear Dynamic Inversion

The incremental form of NDI computes the control increment with respect to the condition of the system one incremental time instance in the past. The fundamental difference with classical NDI is that the control-independent part of the model equations is replaced by state derivative feedback, resulting in a more robust control solution with respect to model mismatch ($\boldsymbol{p}^* \neq \boldsymbol{p}$).[10]

As a first step, the nonlinear system in Equation (1) is approximated by a first-order Taylor series expansion around the current point in time '0':

$$\dot{\boldsymbol{x}} \approx \dot{\boldsymbol{x}}_0 + \left.\frac{\partial}{\partial \boldsymbol{x}}\big(\boldsymbol{f}(\boldsymbol{x}, \boldsymbol{p}) + \boldsymbol{G}(\boldsymbol{x}, \boldsymbol{p})\boldsymbol{u}\big)\right|_{\substack{\boldsymbol{x}=\boldsymbol{x}_0 \\ \boldsymbol{u}=\boldsymbol{u}_0}} \underbrace{(\boldsymbol{x} - \boldsymbol{x}_0)}_{\Delta \boldsymbol{x}} + \left.\frac{\partial}{\partial \boldsymbol{u}}\big(\boldsymbol{f}(\boldsymbol{x}, \boldsymbol{p}) + \boldsymbol{G}(\boldsymbol{x}, \boldsymbol{p})\boldsymbol{u}\big)\right|_{\substack{\boldsymbol{x}=\boldsymbol{x}_0 \\ \boldsymbol{u}=\boldsymbol{u}_0}} \underbrace{(\boldsymbol{u} - \boldsymbol{u}_0)}_{\Delta \boldsymbol{u}} \tag{8}$$

The variables with subscript '0' should be interpreted as an incremental time instance before the equivalent variables without subscript. It assumed that the time-scale separation principle holds for Equation (8). For

very small time increments and instantaneous control effectors, the change in input is much faster than the change in state (i.e. $\boldsymbol{x} - \boldsymbol{x}_0 \approx 0$ while $\boldsymbol{u} - \boldsymbol{u}_0 \neq 0$). Assuming $\boldsymbol{x} - \boldsymbol{x}_0 = 0$, Equation (8) reduces to:

$$\dot{\boldsymbol{x}} \approx \dot{\boldsymbol{x}}_0 + \boldsymbol{G}(\boldsymbol{x}_0, \boldsymbol{p})\Delta\boldsymbol{u} \tag{9}$$

It is assumed that $\boldsymbol{G}$ is non-singular and that $\boldsymbol{y} = \boldsymbol{x}$. In this case INDI can be applied to Equation (9).[10] Defining the virtual control input as $\boldsymbol{\nu} = \dot{\boldsymbol{x}}$ and inverting Equation (9), the following control law is obtained:

$$\Delta\boldsymbol{u} = \boldsymbol{G}^{-1}(\hat{\boldsymbol{x}}_0, \boldsymbol{p}^*)(\boldsymbol{\nu} - \hat{\dot{\boldsymbol{x}}}_0) \tag{10}$$

The vector $\hat{\dot{\boldsymbol{x}}}_0$ contains the state derivatives computed or estimated from $\boldsymbol{y}$ or $\boldsymbol{y}_o$, respectively. Substituting the control law (Equation (10)) into Equation (9):

$$\dot{\boldsymbol{x}} \approx \dot{\boldsymbol{x}}_0 + \boldsymbol{G}(\boldsymbol{x}_0, \boldsymbol{p})\big(\boldsymbol{G}^{-1}(\hat{\boldsymbol{x}}_0, \boldsymbol{p}^*)(\boldsymbol{\nu} - \hat{\dot{\boldsymbol{x}}}_0)\big) \tag{11}$$

In the ideal case ($\hat{\boldsymbol{x}}_0 = \boldsymbol{x}_0$, $\hat{\dot{\boldsymbol{x}}}_0 = \dot{\boldsymbol{x}}_0$ and $\boldsymbol{p}^* = \boldsymbol{p}$), the input-output response approximates to a set of integrators:

$$\dot{\boldsymbol{x}} \approx \boldsymbol{\nu} \quad \Leftrightarrow \quad \boldsymbol{x}(t) \approx \int_0^t \boldsymbol{\nu}(\tau)\mathrm{d}\tau \tag{12}$$

The total input $\boldsymbol{u}$ is obtained by adding the current input $\boldsymbol{u}_0$ to the control increment $\Delta\boldsymbol{u}$. Note that the control law should be sampled with a sufficiently high frequency (100 Hz in this application) and requires synchronization between $\boldsymbol{u}_0$ and $\dot{\boldsymbol{x}}_0$.[12,14]

C. Pseudo Control Hedging

(I)NDI inverts the dynamics of the nonlinear system but not of the input. Actuator dynamics are usually considered time-scale separated from the aircraft dynamics. Saturation caused by the physical limits on actuator position and rate may howhever result in invertibility and controllability issues, violating conditions necessary for dynamic inversion.

Pseudo Control Hedging (PCH) aims to compensate for actuator dynamics by means of modification of the reference model dynamics.[19] PCH scales down (hedges) the reference model signal by an estimate of the response deficiency of the system $\boldsymbol{\nu}_h$, effectively hiding the actuator dynamics from the error dynamics. The virtual control hedge $\boldsymbol{\nu}_h$ is computed by subtracting the commanded virtual control $\boldsymbol{\nu}$ from the actual virtual control $\hat{\boldsymbol{\nu}}$:

$$\boldsymbol{\nu}_h = \boldsymbol{\nu} - \hat{\boldsymbol{\nu}} \tag{13}$$

This concept can be applied to the (I)NDI control laws formulated in Equations (5) and (10). Due to actuator limitations, the commanded control deflections $\boldsymbol{u}$ are not identical to the actual control deflections $\boldsymbol{\delta}$. Rearranging Equations (5) and (10) for $\boldsymbol{\nu}$, $\hat{\boldsymbol{\nu}}$ is obtained by inserting $\boldsymbol{\delta}$ for $\boldsymbol{u}$. For NDI the virtual control hedge is then obtained as follows:

$$\boldsymbol{\nu}_h = L_{\boldsymbol{f}}\boldsymbol{h}(\boldsymbol{x}, \boldsymbol{p}) + L_{\boldsymbol{G}}\boldsymbol{h}(\boldsymbol{x}, \boldsymbol{p})\boldsymbol{u} - \big(L_{\boldsymbol{f}}\boldsymbol{h}(\boldsymbol{x}, \boldsymbol{p}) + L_{\boldsymbol{G}}\boldsymbol{h}(\boldsymbol{x}, \boldsymbol{p})\boldsymbol{\delta}\big) \tag{14}$$

$$\boldsymbol{\nu}_h = L_{\boldsymbol{G}}\boldsymbol{h}(\hat{\boldsymbol{x}}, \boldsymbol{p}^*)(\boldsymbol{u} - \hat{\boldsymbol{\delta}}) \tag{15}$$

A similar result is obtained for INDI:[12]

$$\boldsymbol{\nu}_h = \dot{\boldsymbol{x}}_0 + \boldsymbol{G}(\boldsymbol{x}_0, \boldsymbol{p})(\boldsymbol{u} - \boldsymbol{\delta}_0) - \big(\dot{\boldsymbol{x}}_0 + \boldsymbol{G}(\boldsymbol{x}_0, \boldsymbol{p})(\boldsymbol{\delta} - \boldsymbol{\delta}_0)\big) \tag{16}$$

$$\boldsymbol{\nu}_h = \boldsymbol{G}(\hat{\boldsymbol{x}}_0, \boldsymbol{p}^*)(\boldsymbol{u} - \hat{\boldsymbol{\delta}}) \tag{17}$$

Note that $\boldsymbol{\nu}_h$ only depends on the control effectiveness and that $\boldsymbol{\delta}$ is assumed observable. For a conventional first-order reference model, the hedged output is obtained as follows:

$$\boldsymbol{x}_{ref} = \frac{1}{s}\big(\boldsymbol{K}_{ref}(\boldsymbol{x}_{com} - \boldsymbol{x}_{ref}) - \boldsymbol{\nu}_h\big) \tag{18}$$

Where $\boldsymbol{K}_{ref}$ is the diagonal gain matrix. Note that if $\hat{\boldsymbol{x}}_0 \neq \boldsymbol{x}_0$, $\boldsymbol{p}^* \neq \boldsymbol{p}$ or $\hat{\boldsymbol{\delta}} \neq \boldsymbol{\delta}$, PCH will introduce additional uncertainties into the closed loop system.

III. Research platform

A. Cessna Citation II PH-LAB

The Cessna Citation II PH-LAB is the main research aircraft operated by the Faculty of Aerospace Engineering of Delft University of Technology. Originally designed as a 8-passenger business jet, the PH-LAB has been extensively modified to serve as a multipurpose airborne research platform. The aircraft is powered by two Pratt and Whitney JT15D-4 turbofan engines each providing 11 kN of thrust. The maximum cruise speed is 385 kt and the operating ceiling is 43,000 ft. The PH-LAB is certificated to operate in the restricted category allowing a MTOW of 6622 kg. The aircraft is equipped with numerous facilitates to accommodate flight testing including a Fly-By-Wire (FBW) system,[17] Flight Test Instrumentation System (FTIS), and various sensors.

Figure 1. Laboratory aircraft PH-LAB

Figure 2. Experimental pilot station PH-LAB

1. *FBW system*[17]

The mechanical flight control system of the PH-LAB has been supplemented with an in-house developed electric FBW system. The FBW system is based on the analog autopilot of the aircraft, inheriting all of the safety features and performance limitations associated with this system. The autopilot computer has been modified to accept signals from an experimental FBW computer. Each control channel can be separately controlled by the original autopilot or the FBW computer. The FTIS acts as the main communication hub between the various components of the FBW system. Synchronization and communication between the FTIS and the various software is obtained via the Delft University Environment for Communication and Actuation (DUECA).[23] An important limitation of the FBW system is the restricted control authority due to torque limitations imposed on the actuator servo motors.

A simple controller implemented in the FBW system allows direct command over the deflection angle of the control surfaces. The controller uses a proportional element with the servo motor position as feedback. Note that the transmission ratio between servo motor position and control surface deflection is a function of the force on the actuator cables due to cable stretch.[24] Under quasi-steady airspeed and altitude this ratio can howhever be approximated by a constant.[17]

The starboard cockpit position is designated as the experimental pilot station and equipped with a force sensing side-stick allowing two-axis manual control over the FBW system, see Figure 2. A programmable display provides visualization of the flight instruments and task specific information. Note that no manipulator is available to control the third axis via the FBW system.

2. *Sensors*

Inertial and air data are available from the Attitude Heading and Reference System (AHRS) and Digital Air Data Computer (DADC). The PH-LAB is also equipped with control surface deflection sensors. For this flight test campaign, the aircraft is fitted with an air data boom with vane-type angle of attack and sideslip sensors. Note that the angle of attack is also measured by a body-mounted vane sensor. All sensors all connected to the FTIS allowing in-flight monitoring, recording and processing.

The sensor characteristics of the relevant signals have been determined following flight data analysis, see Table 1. Frequency analysis revealed that the airflow direction sensors pick up a 10 Hz disturbance induced by the excitation of the structural eigenmodes of the air data boom. Note that some of the values in Table 1 have been taken from Van 't Veld.[25]

Table 1. Sensor characteristics PH-LAB

Signal	Noise (σ^2)	Bias	Resolution	Delay [ms]	Sampling freq. [Hz]
$p, q, r, \dot{\theta}, \dot{\phi}, \dot{\psi}$ [rad/s]	$4.0 \cdot 10^{-7}$	$3.0 \cdot 10^{-5}$	$6.8 \cdot 10^{-7}$	90	52
θ, ϕ [rad]	$1.0 \cdot 10^{-9}$	$4.0 \cdot 10^{-3}$	$9.6 \cdot 10^{-7}$	90	52
A_x, A_y, A_z [g]	$1.5 \cdot 10^{-5}$	$2.5 \cdot 10^{-3}$	$1.2 \cdot 10^{-4}$	117	52
V_{tas}, V_{cas} [m/s]	$8.5 \cdot 10^{-4}$	2.5	$3.2 \cdot 10^{-2}$	300	16, 8
h [m]	$4.5 \cdot 10^{-3}$	$8.0 \cdot 10^{-3}$	$3.0 \cdot 10^{-1}$	300	16
$\dot{h}$ [m/s]	$5.5 \cdot 10^{-4}$	$4.5 \cdot 10^{-2}$	$8.1 \cdot 10^{-2}$	300	16
M [-]	$1.0 \cdot 10^{-8}$	$7.0 \cdot 10^{-7}$	$6.3 \cdot 10^{-5}$	300	8
$\delta_a, \delta_e, \delta_r$ [rad]	$5.5 \cdot 10^{-7}$	$2.4 \cdot 10^{-3}$	-	$\sim$0	100
$\alpha_{boom}, \beta_{boom}$ [rad]	$7.5 \cdot 10^{-8}$	$1.8 \cdot 10^{-3}$	$9.6 \cdot 10^{-5}$	100	100
α_{body} [rad]	$4.0 \cdot 10^{-10}$	-	$1.0 \cdot 10^{-5}$	280	1000

B. Aircraft model DASMAT

The aircraft model is a high fidelity 6-DOF nonlinear model of the Cessna Citation I. The model was developed in the Delft University Aircraft Simulation Model and Analysis Tool (DASMAT).[26] The Cessna Citation II is a more recent iteration of the Cessna Citation I with increased seating capacity and improved flight performance. The Citation II features more powerful engines, a longer fuselage and longer wings. Despite these differences, the Citation I DASMAT model fits reasonably well to flight data of the Citation II.[27] The Relative Root Mean Square Error (RRMSE) for the longitudinal force and moment coefficients equate to 9% and 13%, respectively. For the lateral force and moment coefficients the RRMSE equals 7% and 9%, respectively.

1. Model equations

The combined translational and rotational dynamics of a rigid-body aircraft over a flat non-rotating earth are described by the Newton-Euler equations:

$$\dot{\boldsymbol{V}} = m^{-1}\big(\boldsymbol{F}_A(\boldsymbol{x}, \boldsymbol{u}, \boldsymbol{p}) + \boldsymbol{F}_T(\boldsymbol{x}, \boldsymbol{u}_o, \boldsymbol{p})\big) - \boldsymbol{\omega} \times \boldsymbol{V} + \mathbb{T}_{bE} \begin{bmatrix} 0 & 0 & g \end{bmatrix}^{\mathrm{T}} \tag{19}$$

$$\dot{\boldsymbol{\omega}} = \boldsymbol{J}(\boldsymbol{p})\big(\boldsymbol{M}_A(\boldsymbol{x}, \boldsymbol{u}, \boldsymbol{p}) + \boldsymbol{M}_T(\boldsymbol{x}, \boldsymbol{u}_o, \boldsymbol{p}) - \boldsymbol{\omega} \times \boldsymbol{J}(\boldsymbol{p})\boldsymbol{\omega}\big) \tag{20}$$

Where $\boldsymbol{V} = [u, v, w]^{\mathrm{T}}$ are the inertial translational velocities and $\boldsymbol{\omega} = [p, q, r]^{\mathrm{T}}$ the angular rates, both in body axis. $\boldsymbol{F}_A$ and $\boldsymbol{M}_A$ are the aerodynamic forces and moments respectively, $\boldsymbol{F}_T$ and $\boldsymbol{M}_T$ are the forces and moments induced by the thrust. The vectors $\boldsymbol{u}$, $\boldsymbol{u}_o$, $\boldsymbol{x}$ and $\boldsymbol{p}$ are the aerodynamic controls, the throttle settings, the air-mass referenced aircraft states and the model parameters, respectively. $\mathbb{T}_{bE}$ is the transformation matrix from the NED frame to the body frame. The aircraft mass is denoted by m and assumed constant, g is the gravitational constant and $\boldsymbol{J}$ the inertia tensor:

$$\boldsymbol{J}(\boldsymbol{p}) = \begin{bmatrix} J_{xx} & 0 & -J_{xz} \\ 0 & J_{yy} & 0 \\ -J_{xz} & 0 & J_{zz} \end{bmatrix} \tag{21}$$

Note that it is assumed that the aircraft is symmetrical in the xy-plane i.e. $J_{xy} = J_{yz} = 0$. The rotational kinematic motion can be expressed in terms of the Euler angular rates following transformation of the body angular rates:

$$\begin{bmatrix}\dot{\phi}\\ \dot{\theta}\\ \dot{\psi}\end{bmatrix} = \mathbb{T}_{\Phi b}\begin{bmatrix}p\\ q\\ r\end{bmatrix} \quad \text{with} \quad \mathbb{T}_{\Phi b} = \begin{bmatrix}1 & \sin(\phi)\tan(\theta) & \cos(\phi)\tan(\theta)\\ 0 & \cos(\phi) & -\sin(\phi)\\ 0 & \sin(\phi)\sec(\theta) & \cos(\phi)\sec(\theta)\end{bmatrix} \tag{22}$$

The aerodynamic forces and moments are defined in terms of their respective coefficients in the stability reference frame:

$$\boldsymbol{F}_A^{s,cg_{ref}}(\boldsymbol{x},\boldsymbol{u},\boldsymbol{p}) = \frac{1}{2}\rho V_{tas}^2 S\begin{bmatrix}-C_D\\ C_Y\\ -C_L\end{bmatrix} \tag{23}$$

$$\boldsymbol{M}_A^{s,cg_{ref}}(\boldsymbol{x},\boldsymbol{u},\boldsymbol{p}) = \frac{1}{2}\rho V_{tas}^2 S\begin{bmatrix}bC_l\\ cC_m\\ bC_n\end{bmatrix} \tag{24}$$

Where ρ is the air density, V_{tas} the true airspeed, b the wing span, $\bar{c}$ the mean aerodynamic chord and S the wing surface area. C_D, C_Y and C_L are the non-dimensional drag, side force and lift coefficients respectively and C_l, C_m and C_n are the non-dimensional moment coefficients. The aerodynamic coefficients are defined in the stability reference frame with cg_{ref} as origin, the aft limit of the aircraft center of gravity. The force and moment equations in body axis with the center of gravity cg as origin are defined as follows:

$$\boldsymbol{F}_A^{b,cg}(\boldsymbol{x},\boldsymbol{u},\boldsymbol{p}) = \mathbb{T}_{sb}^{-1}\boldsymbol{F}_A^{s,cg_{ref}}(\boldsymbol{x},\boldsymbol{u},\boldsymbol{p}) \tag{25}$$

$$\boldsymbol{M}_A^{b,cg}(\boldsymbol{x},\boldsymbol{u},\boldsymbol{p}) = \mathbb{T}_{sb}^{-1}\boldsymbol{M}_A^{s,cg_{ref}}(\boldsymbol{x},\boldsymbol{u},\boldsymbol{p}) + (\boldsymbol{r}_{cg_{ref}} - \boldsymbol{r}_{cg}) \times \boldsymbol{F}_A^{b,cg}(\boldsymbol{x},\boldsymbol{u},\boldsymbol{p}) \tag{26}$$

Where $\mathbb{T}_{sb}$ is the rotation matrix from the body to the stability reference frame, $\boldsymbol{r}_{cg_{ref}}$ and $\boldsymbol{r}_{cg}$ are the reference and actual position of the center of gravity, respectively.

2. Aerodynamic model

The non-dimensional aerodynamic force and moment coefficients are modeled as ordinary polynomials. As an example, the lateral moment coefficients are parametrized as follows:

$$C_l = C_{l_\beta}\beta + C_{l_{\delta_a}}\delta_a + C_{l_{\delta_r}}\delta_r + C_{l_p}\frac{pb}{2V_{tas}} + C_{l_r}\frac{rb}{2V_{tas}} \tag{27}$$

$$C_n = C_{n_\beta}\beta + C_{n_{\delta_a}}\delta_a + C_{n_{\delta_r}}\delta_r + C_{n_p}\frac{pb}{2V_{tas}} + C_{n_r}\frac{rb}{2V_{tas}} \tag{28}$$

Terms like C_{l_β} may in turn depend on the angle of attack, Mach number, altitude etc. Multiplicative uncertainties are added to the aerodynamic coefficients and the rotational inertia. As an example, the perturbed side force coefficient $\widetilde{C}_Y$ is defined as follows:

$$\widetilde{C}_Y = C_Y(1 + \Delta C_Y) \tag{29}$$

Where C_Y is the nominal value of the side force coefficient and ΔC_Y the corresponding tolerance parameter. These are up to 10% for the longitudinal coefficients and up to 30% for the lateral coefficients following standard practice, see Table 2.

3. Mass model

A highly accurate mass model for the Cessna Citation II is adopted from De Visser.[28] The model is based on the weight and balance calculation procedure of the Citation II and takes into account the mass and position of passengers, payload and fuel. The contribution of the fuel mass is updated by means of feedback of the used fuel and a model of the geometry of the fuel tanks.

4. Sensor models

The following sensor characteristics are modeled: noise, bias, delay and quantization effects (see Table 1). The noise is modeled as a zero-mean Gaussian process. In addition, kinematic position errors are applied on the specific force and airflow direction signals. The disturbances induced by the flexibility of the air data boom are modeled as a 10 Hz sinusoidal signal.

5. Actuator model

A first-order model of the PH-LAB actuator system was developed using available flight data. The flight data contains responses to a series of open loop 3211 and doublet commands applied by the autopilot on elevator and aileron. Besides a first-order lag component, the model includes actuator position and rate limits, and a transport delay:

$$\dot{\delta}(t) = S_{\dot{\delta}}\Big(K_{fbw}\omega_{act}u(t-\tau_{act}) - \omega_{act}S_{\delta}\big(\delta(t)\big)\Big) \qquad (30)$$

Where S_δ and $S_{\dot{\delta}}$ are the saturation function for actuator position and rate, respectively. K_{fbw} is the FBW input-output gain i.e. the transmission ratio between servo motor position and control surface deflection. The actuator bandwidth ω_{act} and transport delay τ_{act} are determined by fitting the measured control deflections to the general step input time response of a first-order system. A nonlinear least square curve-fitting method was used to find the optimum fit. For each step input command the maximum rate of deflection $\dot{\delta}_{max}$ was determined as well.

Table 2. PH-LAB parameter uncertainty ranges

Symbol	Minimum	Nominal	Maximum
$\Delta\tau_{sync}$	−0.3	0	0.3
ΔJ_{xx}	−0.1	0	0.1
ΔJ_{yy}	−0.1	0	0.1
ΔJ_{yy}	−0.1	0	0.1
ΔJ_{xz}	−0.3	0	0.3
ΔC_D	−0.1	0	0.1
ΔC_L	−0.3	0	0.3
ΔC_Y	−0.1	0	0.1
ΔC_{l_β}	−0.3	0	0.3
ΔC_{m_0}	−0.1	0	0.1
ΔC_{n_β}	−0.3	0	0.3
ΔC_{l_p}	−0.3	0	0.3
ΔC_{l_r}	−0.3	0	0.3
ΔC_{m_q}	−0.1	0	0.1
ΔC_{n_p}	−0.3	0	0.3
ΔC_{n_r}	−0.3	0	0.3
$\Delta C_{l_{\delta_a}}$	−0.3	0	0.3
$\Delta C_{l_{\delta_r}}$	−0.3	0	0.3
$\Delta C_{m_{\delta_e}}$	−0.1	0	0.1
$\Delta C_{n_{\delta_a}}$	−0.3	0	0.3
$\Delta C_{n_{\delta_r}}$	−0.3	0	0.3

Table 3. Actuator model parameters

	δ_{max} [deg]	δ_{min} [deg]	K_{fbw} [-]	$\dot{\delta}_{max}$ [deg/s]	τ_{act} [ms]	ω_{act} [rad/s]
Aileron	15	-19	0.70	19.7 ($\sigma = 4.81$)	39.8 ($\sigma = 7.91$)	12.4 ($\sigma = 2.30$)
Elevator	15	-17	0.60			
Rudder	22	-22	0.55			

IV. Control law design

For the controller developed in this paper two control objectives are formulated: Rate Control Attitude Hold (RCAH) and Attitude Control (AC).[18] RCAH is governed between ±27° and ±15° for roll and pitch, respectively. AC is governed outside this range up to ±35° and ±20° for roll and pitch, respectively. The lateral tracking task includes the angle of sideslip as well. The general controller structure can be found in Figure 3.

A. Inner loop

(I)NDI is applied to the rotational dynamics of the aircraft. The control variables $\boldsymbol{y}$ are set equal to the body angular rates $\boldsymbol{\omega} = [p, q, r]^{\mathrm{T}}$. The aileron, elevator and rudder deflection are selected as input, i.e. $\boldsymbol{u} = [\delta_a, \delta_e, \delta_r]^{\mathrm{T}}$.

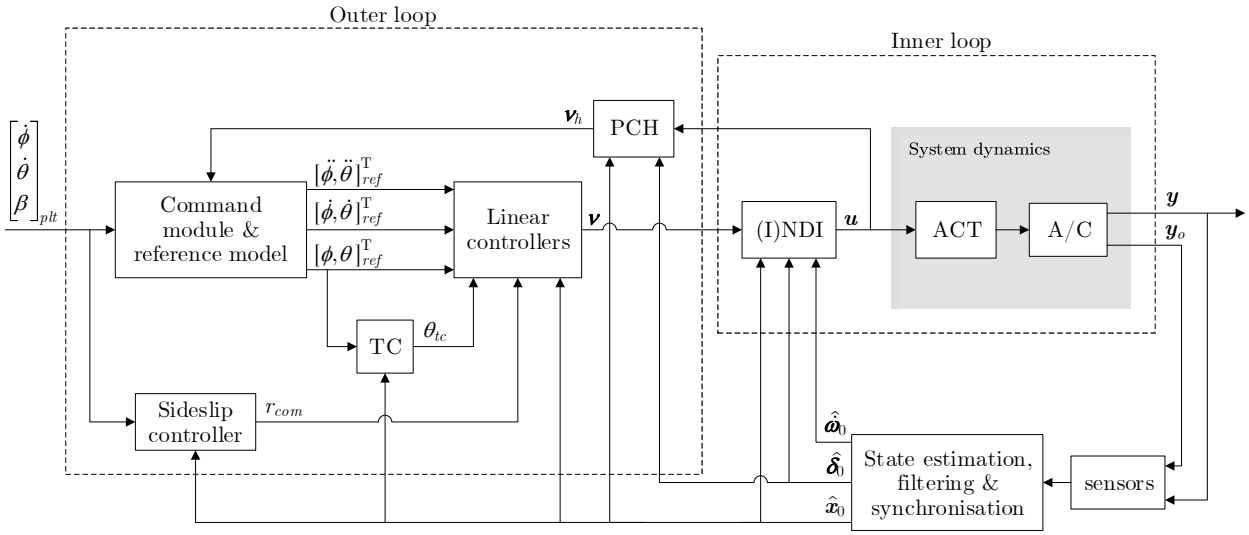

Figure 3. General controller structure

1. *Angular rate NDI*

The analytic relationship between the body angular rates and control surface deflections arises directly from Euler's rotation equations, see Equation (20). Neglecting the moment induced by the thrust $\boldsymbol{M}_T$, the aerodynamic moment $\boldsymbol{M}_A$ can be split into into an airframe dependent part $\boldsymbol{M}_a$ and a part dependent on the control effectors $\boldsymbol{M}_c$. These are assumed to be of the following form:

$$\boldsymbol{M}_a(\boldsymbol{x},\boldsymbol{p}) = \frac{1}{2}\rho V_{tas}^2 S \begin{bmatrix} bC_{l_a} \\ \bar{c}C_{m_a} \\ bC_{n_a} \end{bmatrix} \tag{31}$$

$$\frac{\partial \boldsymbol{M}_c(\boldsymbol{x},\boldsymbol{p},\boldsymbol{u})}{\partial \boldsymbol{u}} = \boldsymbol{M}_{c_{\boldsymbol{\delta}}}(\boldsymbol{x},\boldsymbol{p}) = \frac{1}{2}\rho V_{tas}^2 S \begin{bmatrix} bC_{l_{\delta_a}} & 0 & bC_{l_{\delta_r}} \\ 0 & \bar{c}C_{m_{\delta_e}} & 0 \\ bC_{n_{\delta_a}} & 0 & bC_{n_{\delta_r}} \end{bmatrix} \tag{32}$$

Note that it is assumed that $\boldsymbol{M}_c$ is linear in $\boldsymbol{u}$. Equation (20) can be rewritten as follows:

$$\dot{\boldsymbol{\omega}} = \boldsymbol{J}^{-1}(\boldsymbol{p})\big(\boldsymbol{M}_a(\boldsymbol{x},\boldsymbol{p}) + \boldsymbol{M}_{c_{\boldsymbol{\delta}}}(\boldsymbol{x},\boldsymbol{p})\boldsymbol{u} - \boldsymbol{\omega}\times\boldsymbol{J}(\boldsymbol{p})\boldsymbol{\omega}\big) \tag{33}$$

Applying dynamic inversion to Equation (33), the following control law is obtained:

$$\boldsymbol{u} = \underbrace{\boldsymbol{M}_{c_{\boldsymbol{\delta}}}^{-1}(\hat{\boldsymbol{x}},\boldsymbol{p}^*)\boldsymbol{J}(\boldsymbol{p}^*)}_{(L_{\boldsymbol{G}}\boldsymbol{h})^{-1}}\Big(\boldsymbol{\nu} - \underbrace{\boldsymbol{J}^{-1}(\boldsymbol{p}^*)\big(\boldsymbol{M}_a(\hat{\boldsymbol{x}},\boldsymbol{p}^*) - \boldsymbol{\omega}\times\boldsymbol{J}(\boldsymbol{p}^*)\boldsymbol{\omega}\big)}_{L_{\boldsymbol{f}}\boldsymbol{h}}\Big) \tag{34}$$

2. *Angular rate INDI*

The incremental form of Euler's rotation equation is obtained following a first-order Taylor expansion of Equation (33) around the current point in time '0':

$$\begin{aligned}\dot{\boldsymbol{\omega}} \approx \dot{\boldsymbol{\omega}}_0 &+ \frac{\partial}{\partial\boldsymbol{\omega}}\Big(\boldsymbol{J}^{-1}(\boldsymbol{p})\big(\boldsymbol{M}_a(\boldsymbol{x},\boldsymbol{p}) + \boldsymbol{M}_{c_{\boldsymbol{\delta}}}(\boldsymbol{x},\boldsymbol{p})\boldsymbol{u} - \boldsymbol{\omega}\times\boldsymbol{J}(\boldsymbol{p})\boldsymbol{\omega}\big)\Big)\Big|_{\substack{\boldsymbol{\omega}=\boldsymbol{\omega}_0\\ \boldsymbol{u}=\boldsymbol{u}_0}} \underbrace{(\boldsymbol{\omega}-\boldsymbol{\omega}_0)}_{\Delta\boldsymbol{\omega}} \\ &+ \frac{\partial}{\partial\boldsymbol{u}}\Big(\boldsymbol{J}^{-1}(\boldsymbol{p})\big(\boldsymbol{M}_a(\boldsymbol{x},\boldsymbol{p}) + \boldsymbol{M}_{c_{\boldsymbol{\delta}}}(\boldsymbol{x},\boldsymbol{p})\boldsymbol{u} - \boldsymbol{\omega}\times\boldsymbol{J}(\boldsymbol{p})\boldsymbol{\omega}\big)\Big)\Big|_{\substack{\boldsymbol{\omega}=\boldsymbol{\omega}_0\\ \boldsymbol{u}=\boldsymbol{u}_0}} \underbrace{(\boldsymbol{u}-\boldsymbol{u}_0)}_{\Delta\boldsymbol{u}}\end{aligned} \tag{35}$$

Again assuming $\boldsymbol{\omega} - \boldsymbol{\omega}_0 = 0$, Equation (35) reduces to:

$$\dot{\boldsymbol{\omega}} \approx \dot{\boldsymbol{\omega}}_0 + \boldsymbol{J}^{-1}(\boldsymbol{p})\boldsymbol{M}_{c_{\boldsymbol{\delta}}}(\boldsymbol{x}_0, \boldsymbol{p})\Delta\boldsymbol{u} \tag{36}$$

Applying dynamic inversion to Equation (36) and adding the current control surface deflections $\boldsymbol{\delta}_0$, the following control law is obtained:

$$\boldsymbol{u} = \underbrace{\boldsymbol{M}_{c_{\boldsymbol{\delta}}}^{-1}(\hat{\boldsymbol{x}}_0, \boldsymbol{p}^*)\boldsymbol{J}(\boldsymbol{p}^*)}_{\boldsymbol{G}^{-1}}(\boldsymbol{\nu} - \underbrace{\hat{\dot{\boldsymbol{\omega}}}_0}_{\hat{\boldsymbol{x}}_0}) + \hat{\boldsymbol{\delta}}_0 \tag{37}$$

B. Outer loop[18]

The outer loop consists of the following components: command module & reference model, sideslip controller, Turn Compensation (TC), linear controllers and Pseudo Control Hedging (PCH).

1. *Command module & reference model*

The command module and reference model serve as attitude flight envelope protection and command filter, respectively. Furthermore, the command module blends two different control methods: rate control attitude hold (RCAH) and attitude control (AC). RCAH is active between 27° and −27° for roll and between 15° and −15° for pitch. When these limits are reached the feedforward term is deactivated and the pilot command signal is directly added to the saturated signal, see Figure 4. This way the attitude angles are directly governed by the pilot command input. AC is active up to ±35° for roll and ±20° for pitch, these are the limit values of the system. Note that for zero pilot input command in AC mode, the system will always command the aircraft back to the RCAH attitude limits. The purpose of this setup is to reduce violent behavior when the roll and pitch limits of the system are reached. The gain K_2 in the command module is required to achieve a smooth transition between AC and RACH. The reference model is conventional second-order system smoothing the command signals to values achievable by the aircraft, see Equation (38).

$$H_{ref}(s) = \frac{K_1 K_2}{s^2 + K_1 s + K_1 K_2} = \frac{\omega_{n_{ref}}^2}{s^2 + 2\zeta_{ref}\omega_{n_{ref}} s + \omega_{n_{ref}}^2} \tag{38}$$

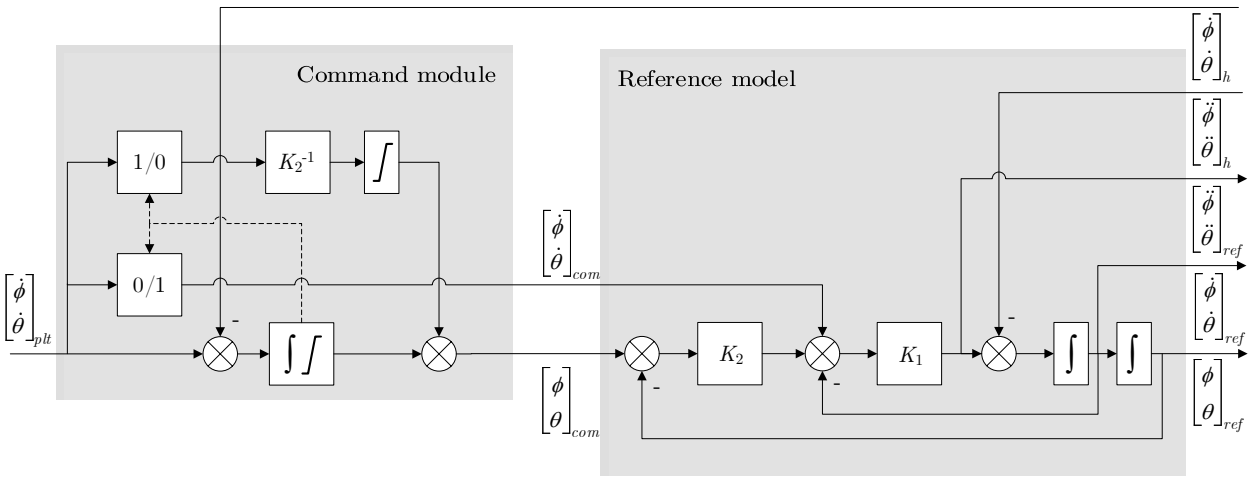

Figure 4. Command module & reference model[18]

2. *Sideslip controller*

For manual control, the angle of sideslip is preferred as outer loop control variable. Furthermore, as there is no means to manually control the yaw axis due to absence of a yaw input device, coordinated flight is only possible by means of direct sideslip augmentation. The control setup therefore includes a sideslip controller:

$$r_{com} = \frac{1}{V_{tas}}(wp - A_y) - \left(\frac{1}{s}K_{\beta_I}(\beta_{plt} - \beta) - K_\beta \beta\right) \quad \text{with} \quad w \approx V_{tas}\alpha \tag{39}$$

3. Turn Compensation

The control setup includes a turn compensation (TC) module with the following control law:

$$\theta_{tc} = \big(\cos(\phi_{ref}) - 1\big)\frac{mg}{\frac{1}{2}\rho_0 V_{cas}^2 S C_{L_\alpha}} \tag{40}$$

4. Linear controllers

The linear controllers are defined in Equations (41) to (43). For the pitch and roll channel, the controllers operate up to the 2nd order time derivative.

$$\nu_{\dot{\phi}} = \left(K_\phi + \frac{K_{\phi_I}}{s}\right)(\phi_{ref} - \phi) + K_{\dot{\phi}}(\dot{\phi}_{ref} - \dot{\phi}) + K_{\ddot{\phi}}\ddot{\phi}_{ref} \tag{41}$$

$$\nu_{\dot{\theta}} = \left(K_\theta + \frac{K_{\theta_I}}{s}\right)(\theta_{ref} + \theta_{tc} - \theta) + K_{\dot{\theta}}(\dot{\theta}_{ref} - \dot{\theta}) + K_{\ddot{\theta}}\ddot{\theta}_{ref} \tag{42}$$

$$\nu_r = K_r(r_{com} - r) \tag{43}$$

Kinematic inversion of Equations (41) and (42) immediately results in:

$$\begin{bmatrix}\nu_p\\ \nu_q\\ \nu_r\end{bmatrix} = \mathbb{T}_{\Phi b}^{-1}\begin{bmatrix}\nu_{\dot{\phi}}\\ \nu_{\dot{\theta}}\\ \nu_{\dot{\psi}}\end{bmatrix} - \dot{\mathbb{T}}_{\Phi b}\begin{bmatrix}p\\ q\\ r\end{bmatrix} \tag{44}$$

5. Pseudo Control Hedging

Pseudo Control Hedging is implemented slightly differently as in Lombaearts and Looye,[18] where hedging was only activated upon saturation of the actuator model. As the PH-LAB actuator model does not include speed dependent position limiting, activation upon model saturation is not desirable. In this setup, upon manual activation, compensation will be provided irrespective of actuator saturation.

Consider again Equation (17), substituting the above result obtained for $\boldsymbol{G}$, the virtual control hedge $\boldsymbol{\nu}_h$ is obtained as follows:

$$\boldsymbol{\nu}_h = \underbrace{\boldsymbol{M}_{c_{\boldsymbol{\delta}}}(\hat{\boldsymbol{x}}_0, \boldsymbol{p}^*)\boldsymbol{J}^{-1}(\boldsymbol{p}^*)}_{\boldsymbol{G}}(\boldsymbol{u} - \hat{\boldsymbol{\delta}}) \tag{45}$$

Kinematic inversion of Equation (45) immediately results in:

$$\begin{bmatrix}\nu_{\dot{\phi}}\\ \nu_{\dot{\theta}}\\ \nu_{\dot{\psi}}\end{bmatrix}_h = \mathbb{T}_{\Phi b}\begin{bmatrix}\nu_p\\ \nu_q\\ \nu_r\end{bmatrix}_h + \dot{\mathbb{T}}_{\Phi b}\begin{bmatrix}p\\ q\\ r\end{bmatrix} \tag{46}$$

The compensation signal is subtracted from the reference signal $[\ddot{\phi}_{ref}, \ddot{\theta}_{ref}]^{\mathrm{T}}$, see Figure 4. The command module also requires hedging as the commanded attitude $[\phi_{com}, \theta_{com}]^{\mathrm{T}}$ is obtained via integration of the pilot rate command $[\dot{\phi}_{plt}, \dot{\theta}_{plt}]^{\mathrm{T}}$, leaving the commanded attitude unhedged would lead to undesired overshoot.

C. State estimation, filtering and synchronisation

Good quality sensor signals are imperative to (I)NDI control. Not all signals provided by the PH-LAB sensor systems are processed and might contain disturbances that would propagate through the control laws without filtering. Inertial sensors are sensitive to structural vibrations while air data sensors pick up atmospheric turbulence. The flexibility of the PH-LAB air data boom also adds a 10 Hz disturbance to the airflow direction signals. The filtering techniques proposed here are in part taken from Looye and Joos.[29]

The angular acceleration signals require additional attention as these are obtained via differentiation. Careful filtering of the angular rates is necessary to reduce sensor noise. The angular rate and control deflection signals also require synchronization.

1. Inertial data

The angular rates are filtered with a second-order low-pass filter:[9]

$$H_{fil}(s) = \frac{\omega_{n_{fil}}^2}{s^2 + 2\zeta_{fil}\omega_{n_{fil}} + \omega_{n_{fil}}^2} \tag{47}$$

The natural frequency $\omega_{n_{fil}}$ is set equal to 20 rad/s and the damping ratio ζ_{fil} is unity. The remainder of the inertial signals are filtered using first-order low-pass filters with a time constant of 50 ms.

2. Air data

All DADC and airflow direction signals are combined with inertial measurements using a first-order complementary filter:

$$\hat{x} = \frac{1}{\tau_{fil}s + 1}x + \frac{\tau_{fil}s}{\tau_{fil}s + 1}x_i \tag{48}$$

Where x_i is the inertial equivalent of air data signal x. The filter time constant τ_{fil} is set equal to 1 s. Note that for some signals the derivative of the inertial signal is used as high-pass signal.

The inertial speed $\dot{V}_i$ is calculated from the linear accelerations:

$$\dot{V}_i = \begin{bmatrix} a_x & a_y & a_z \end{bmatrix} \begin{bmatrix} \cos(\alpha)\cos(\beta) \\ \sin(\beta) \\ \sin(\alpha)\cos(\beta) \end{bmatrix} \quad \text{with} \quad \begin{bmatrix} a_x \\ a_y \\ a_z \end{bmatrix} = g \left(\begin{bmatrix} A_x \\ A_y \\ A_z \end{bmatrix} + \begin{bmatrix} -\sin(\theta) \\ \cos(\theta)\sin(\phi) \\ \cos(\theta)\cos(\phi) \end{bmatrix} \right) \tag{49}$$

The derivative of the inertial vertical speed $\ddot{h}_i$ is also obtained from the linear accelerations:

$$\ddot{h}_i = \begin{bmatrix} a_x & a_y & a_z \end{bmatrix} \begin{bmatrix} \sin(\theta) \\ -\cos(\theta)\sin(\phi) \\ -\cos(\theta)\cos(\phi) \end{bmatrix} \tag{50}$$

The altitude h is complemented with the complementary filtered vertical speed $\hat{\dot{h}}$. An approximation is used for the inertial Mach number M_i:

$$M_i \approx \frac{V_{tas}}{20.05\sqrt{(288.2 - 0.0065h)}} \tag{51}$$

The inertial angle of attack α_i is computed as follows:

$$\alpha_i = \theta - \gamma_a \quad \text{with} \quad \gamma_a \approx \frac{\dot{h}}{V_{tas}} \tag{52}$$

The derivative of the inertial angle of sideslip $\dot{\beta}_i$ is obtained as follows:

$$\dot{\beta}_i = \frac{A_y g + g\sin(\phi)\cos(\theta)}{V_{tas}} - r\cos(\alpha) + p\sin(\alpha) \tag{53}$$

3. Control deflections

Synchronization between control deflection and angular acceleration feedback is achieved by applying equivalent filtering and artificially adding the surplus of angular rate delay to the control deflection signal:[14,15]

$$\hat{\boldsymbol{\delta}}_0 = H_{fil}(s)H_{sync}(s)\boldsymbol{\delta} \tag{54}$$

Where H_{sync} is the frequency-domain equivalent of a pure time delay τ_{sync} corresponding to the surplus of angular rate delay. To account for variations in delay (e.g. due to sampling or unmodeled delays), a multiplicative uncertainty is added to τ_{sync}. Alternatively, the synchronized control deflections may be estimated using actuator models:

$$\hat{\boldsymbol{\delta}}_{0_{est}} = \frac{z^{-1}H_{act}(s)H_{fil}(s)H_{sync}(s)}{1 - z^{-1}H_{act}(s)H_{fil}(s)H_{sync}(s)}\Delta\boldsymbol{u} \tag{55}$$

Where H_{act} represents the actuator dynamics i.e. the frequency-domain equivalent of Equation (30). Note that z^{-1} is the increment delay, strictly this term is required as $\Delta\boldsymbol{u}$ is one incremental time step ahead of $\boldsymbol{\delta}_0$.

D. Design optimization

For the tuning of the control laws multi-objective optimization is used. The Institute of System Dynamics and Control (SR) of the German Aerospace Institute (DLR) developed the Multi-Objective Parameter Synthesis (MOPS) tool specifically for this purpose.[30] Robustness is addressed via a multi-model approach and unspecific robustness criteria.[29] The tuning of the lateral and longitudinal controller parameters are performed separately, the discussion will be limited to the lateral case only.

1. Design criteria

Multi-objective optimization requires a set of computable criteria that can be used for optimization. The design criteria for the lateral synthesis parameters are defined in Table 4. These are computed from three nonlinear simulations and a linear analysis of the closed-loop system. Simulations 1 and 2 are used to evaluate the reference tracking with criteria concerning overshoot, rise time, settling time and control effort. Simulation 3 is used to assess the disturbance rejection by means of a cross-wind step.

The criteria are formulated as min-max optimization problems and scaled such that a value smaller than 1 is considered satisfactory. The criteria corresponding to the nonlinear simulations are scaled by division of the corresponding demand value. The criteria corresponding to the linear analysis are scaled using 'good-bad' values.[30] With this scaling type, it is demanded that the criterion is at least equal to the 'bad-low' value. The region between 'bad-low' and 'good-low' is considered acceptable with linearly decreasing scaling. Values larger than 'good low' are considered equally good and are subsequently scaled to 0. Notice that for some of the criteria in Table 4 an inequality constraint is used such that no further optimization is performed after the demand value is obtained.

2. Robustness

The robustness of the control law is addressed in two ways. A multi-model approach is used to achieve robustness to parametric uncertainties. The multi-model setup is created by adding a number of model cases with worst-case parameter combinations to the nominal case. These worst-cases are defined with respect to one of the design criteria defined in Table 4. The optimization process addresses the criteria simultaneously for all model cases allowing for trade-off between criteria under worst-case and nominal parameter conditions. Note that this approach implicitly assumes that the controller is also robust to model cases in between those addressed. To this end also local robustness margins are included as optimization criteria. These are the minimum phase and gain margins at the sensor and actuator positions listed in Table 4. Note that the local robustness criteria are also intended to achieve robustness to unspecified uncertainties (e.g. unmodeled dynamics and time delays).

Table 4. Design criteria lateral part

Name	Description	Calculation	Bad-low	Good-low	Demand	Type
Simulation 1: Box-cart: $\dot{\phi}_{plt} = 5$ °/s at $t = 1$ till $t = 6$ s						
osdphi [-]	Overshoot $\dot{\phi}$		-	-	0.5	c
rtdphi [s]	Rise time $\dot{\phi}$	0%→100%	-	-	0.75	c
stdphi [s]	Settling time $\dot{\phi}$	0.1°	-	-	4	m
osphi [-]	Overshoot ϕ		-	-	0.1	c
rtphi [s]	Rise time ϕ	0%→100%	-	-	5	c
stphi [s]	Settling time ϕ	0.1°	-	-	4	m
maxdda [deg/s]	Maximum $\dot{\delta}_a$	$\max\lvert\dot{\delta}_a\rvert$	-	-	40	m
errbeta [deg]	Error β	$\int_0^T \lvert\beta\rvert \mathrm{d}t/T$	-	-	0.5	m
Simulation 2: Step $\beta_{plt} = 5°$ at $t = 1$ s						
osbeta [-]	Overshoot β		-	-	0.01	c
rtbeta [s]	Rise time β	10%→90%	-	-	4	m
stbeta [s]	Settling time β	0.1°	-	-	5	m
maxddr [deg/s]	Maximum $\dot{\delta}_r$	$\max\lvert\dot{\delta}_r\rvert$	-	-	20	m
errphi [deg]	Error ϕ	$\int_0^T \lvert\phi\rvert \mathrm{d}t/T$	-	-	0.5	m
Simulation 3: Wind step $v_{wind} = 16$ m/s at $t = 1$ s						
maxphi [deg]	Maximum ϕ	$\max\lvert\phi\rvert$	-	-	6.7	m
maxdr [deg]	Maximum δ_r	$\max\lvert\delta_r\rvert$	-	-	22	m
Linear analysis:						
gmda [dB]	Gain margin δ_a		4	6	-	m
pmda [deg]	Phase margin δ_a		30	60	-	c
gmdr [dB]	Gain margin δ_r		4	6	-	m
pmdr [deg]	Phase margin δ_r		30	60	-	c
gmp [dB]	Gain margin p		4	6	-	m
pmp [deg]	Phase margin p		30	60	-	c
gmr [dB]	Gain margin r		4	6	-	m
pmr [deg]	Phase margin r		30	60	-	c
m=minimize, c=inequality constraint						

3. Parameter synthesis

The parameter synthesis was performed in three successive steps. First the linear controller gains and reference model parameters were optimized. With the resulting tuning parameter set, a worst-case analyses was performed. Note that it was assumed that the worst-cases are to be found at the extremities of the parameter space. To this end, minimum or maximum values were selected for the parametric model uncertainties. The criteria were evaluated for all parameter combinations. To limit the number of combinations for NDI, tolerances on the moment of inertia and less relevant aerodynamic coefficients were left out.

The two criteria that proofed most sensitive to parameter variations were added as separate model cases to the nominal model to form a multi-model set. An additional parameter synthesis was performed for this set of model-cases. The results can be found in Table 5. Note that the maximum uncertainty on the lateral moment coefficients has been slightly relieved to 20%, else a satisfactory design for the NDI controller could not be realized.

4. Assessment

The best-compromise solution for INDI and NDI will now be compared. Notice in Table 5 that for INDI a significantly lower integrator gain K_{ϕ_I} was selected by the optimizer compared to NDI. This behaviour can be attributed to the incremental nature of INDI as the calculated increment is added to the current

input, basically acting as an integral term. Further notice that for the worst cases the optimizer pushed the synchronization uncertainty $\Delta\tau_{sync}$ to its minimum value. This behaviour was expected considering that a surplus of state derivative delay results in relatively fast system instability.[25] Steady-state offsets in the angular rate tracking were effectively regulated by the linear controllers. The steady errors in the sideslip tracking are the result of measurement bias. The settling time calculation was subsequently relieved to 0.2°. Note that the noise was deactivated during the optimization as this would cause inconsistencies between the different evaluations. For the NDI worst cases the criteria corresponding to *stdphi*, *stphi*, *osbeta* and *errphi* had to be relieved.

The responses corresponding to the nonlinear simulations can be found in Figures 5 to 7. Note that the blue lines represent the responses of the nominal case and the grey area contains the responses of the worst cases. This area should be interpreted as the design uncertainty. As expected, the responses corresponding to the INDI controller show less sensitivity to parameter variations, with smaller deviations between the cases. The difference is most prominent in Figure 6. The NDI controller is unable to regulate the roll angle error under sideslip for uncertain parameter conditions, with errors up to 1.4°. The incremental controller has superior disturbance rejection compared to NDI, with faster attenuation and lower overshoot in the attitude response, see Figure 7. This result conforms to observations made by Acquentella et al.[11]

Table 5. Synthesis parameters lateral part

Tuning parameter	INDI			NDI		
Linear controller gains:						
K_ϕ	5.51			7.91		
K_{ϕ_I}	1.34			7.02		
$K_{\dot{\phi}}$	4.80			6.48		
$K_{\ddot{\phi}}$	1.05			0.941		
K_r	1.62			3.22		
K_β	1.93			1.55		
K_{β_I}	0.977			0.709		
Reference model parameters:						
ζ_{ref}	1.00			0.741		
$\omega_{n_{ref}}$	1.35			1.27		
Uncertain model parameters:						
	nominal	worst gmda	worst pmp	nominal	worst gmda	worst gmp
$\Delta\tau_{sync}$	0	-0.3	-0.3	0	0	0
ΔJ_{xx}	0	-0.1	-0.1	0	0	0
ΔJ_{zz}	0	-0.1	-0.1	0	0	0
ΔJ_{xz}	0	0.3	-0.3	0	0	0
ΔC_Y	0	0.3	-0.3	0	0.3	0.3
ΔC_{l_β}	0	0	0	0	-0.2	-0.2
$\Delta C_{l_{\delta_a}}$	0	-0.2	0.2	0	0.2	0.2
$\Delta C_{l_{\delta_r}}$	0	0.2	0.2	0	0	0
ΔC_{l_p}	0	0	0	0	-0.2	0.2
ΔC_{l_r}	0	0	0	0	-0.2	-0.2
ΔC_{n_β}	0	0	0	0	-0.2	-0.2
$\Delta C_{n_{\delta_r}}$	0	0.2	0.2	0	0.2	0.2
$\Delta C_{n_{\delta_a}}$	0	0.2	0.2	0	0	0
ΔC_{n_p}	0	0	0	0	-0.2	-0.2
ΔC_{n_r}	0	0	0	0	0.2	-0.2

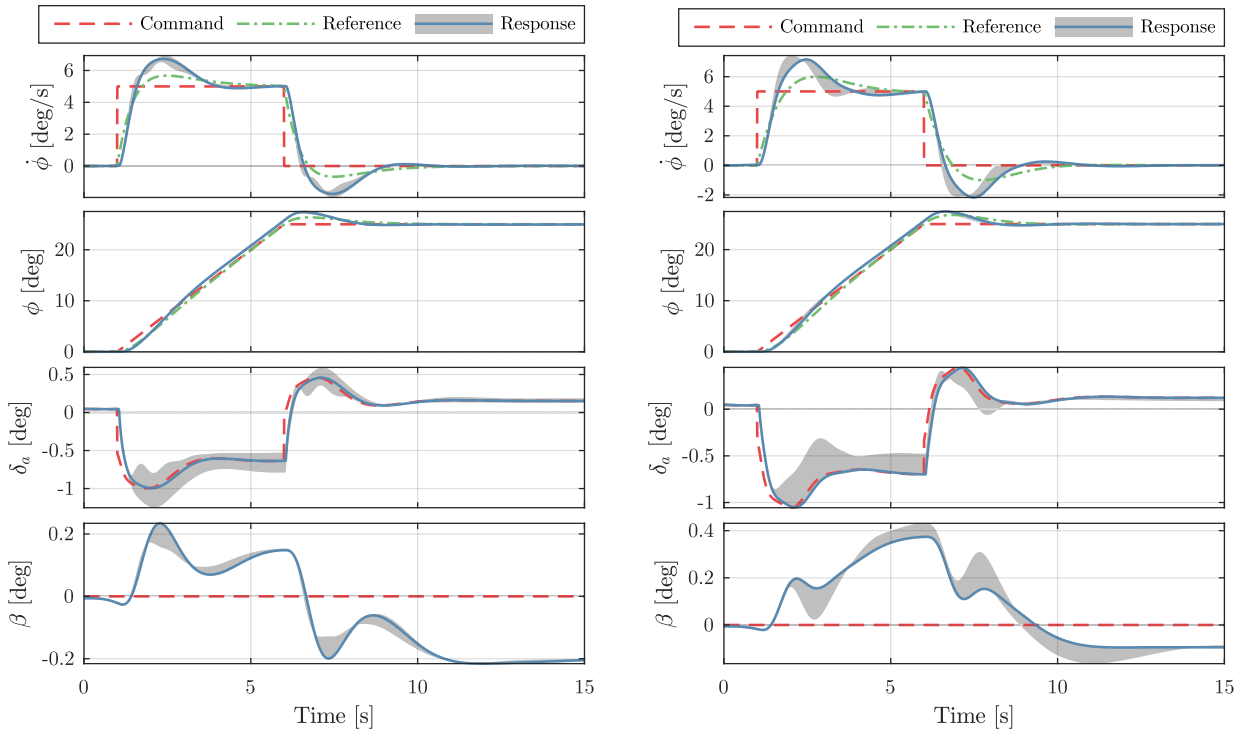

(a) INDI (b) NDI

Figure 5. Simulation 1: tracking response to 5°/s roll rate box-cart

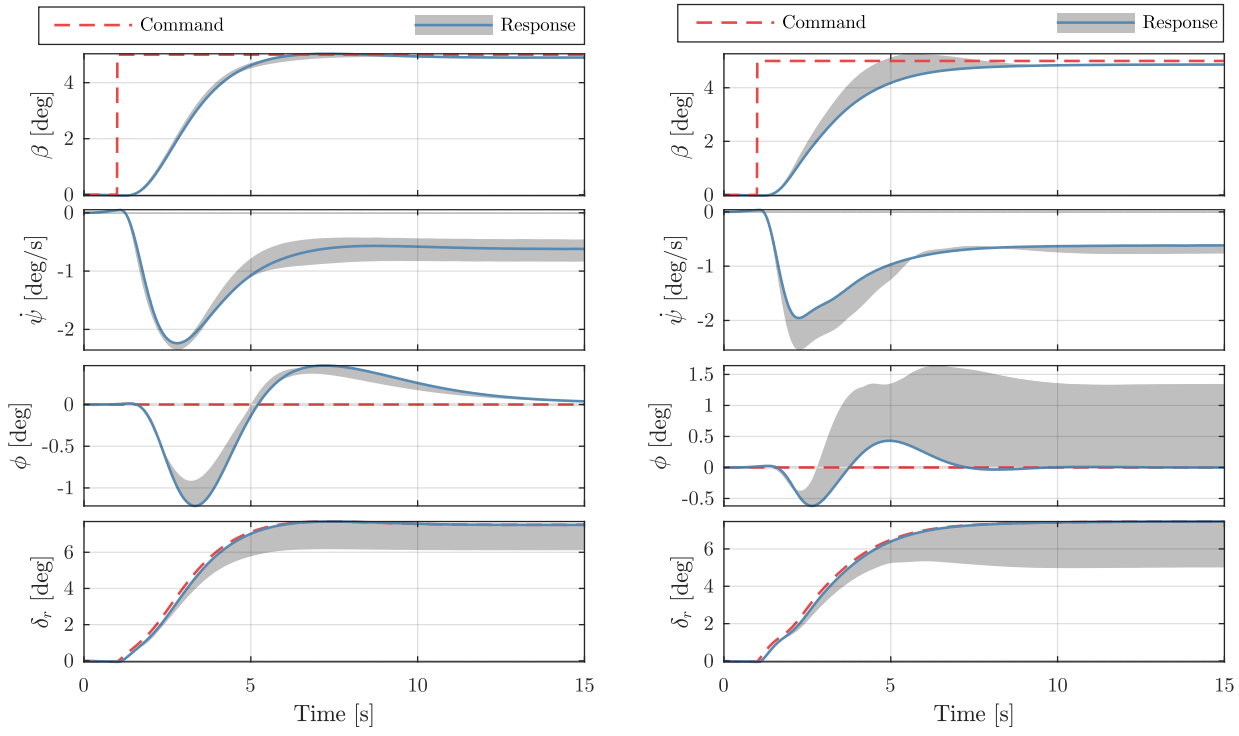

(a) INDI (b) NDI

Figure 6. Simulation 2: tracking response to 5° sideslip step

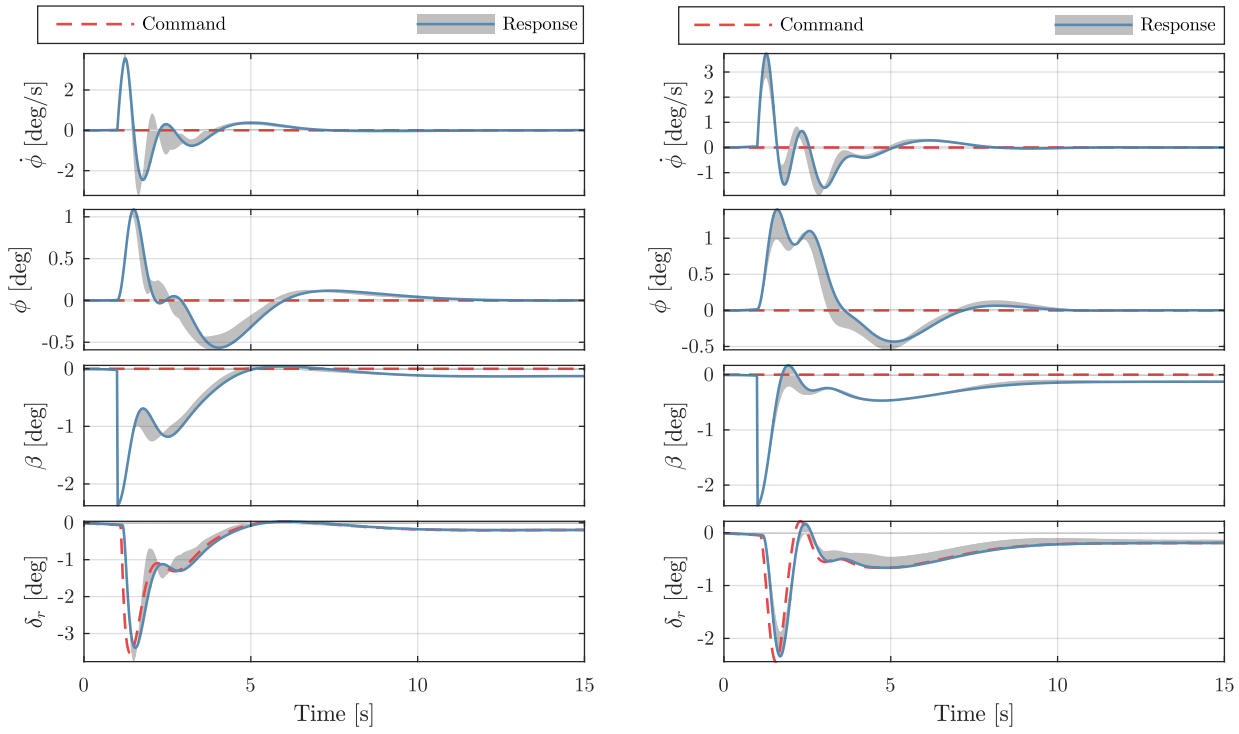

(a) INDI (b) NDI

Figure 7. Simulation 3: tracking response to 16 m/s cross-wind step

V. Control law validation

A. Simulator assessment and clearance

For the assessment and clearance of the experimental controller, use was made of the robotic motion simulator operated by the Institute of System Dynamics and Control (SR) of the German Aerospace Institute (DLR).[31] The simulator utilizes a serial kinematics industrial robot arm to generate motion cues to the attached simulator pod, greatly enlarging the motion capability compared to conventional hexapod simulators. The simulator pod is fully modular allowing use of various instrument consoles. The set-up of the cockpit includes a certified side-stick, dual throttle control system and rudder pedals. Complete three-dimensional cockpit visualization is provided via a virtual reality headset.

Specific attention was paid to the controller behavior at initialization and during switching between different controller modes. These operations should be free of any transients. The pilot-in-the-loop allowed a qualitative assessment of the overall dynamics and handling qualities of the system.

Figure 8. Robotic Motion Simulator DLR

B. Rig testing

Extensive rig testing was performed on the "iron bird" of the PH-LAB. This system includes the actual FBW hardware components and is used to validate proper functioning in interaction of the experimental controller with the system hardware. For software implementation, the Delft University Environment for Communication and Activation (DUECA)[23] is used. This framework allows straightforward implementation of controllers developed in the MATLAB/Simulink environment.

C. Flight tests

Over the course of five days, three successive flight test were performed to validate the incremental controller. All flights departed from and terminated at Amsterdam Airport Schiphol (AMS) and the experiments were executed in designated areas within Dutch airspace, see Figure 9.

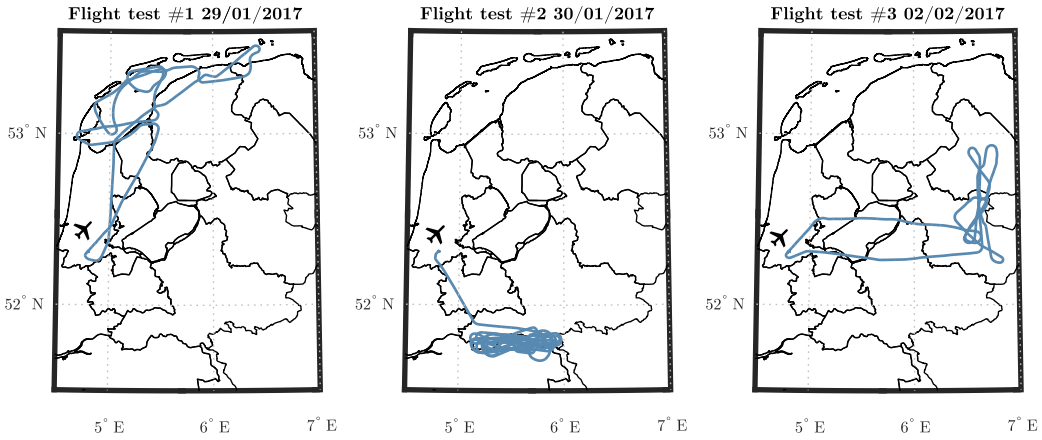

Figure 9. Flight track of test flights

1. *Experimental setup*

The aircraft was configured in a clean setup during the flight tests with gear, flaps and spoilers retracted. The experiments were repeated for two flight conditions: 200 KIAS FL150 and 240 KIAS FL150. The automatic elevator trim was deactivated during most of the experiments. Since the PH-LAB is not fitted with an autothrottle, the safety pilot was tasked to monitor and correct the airspeed manually. The experiments were performed throughout the whole flight.

The experiments focused on a series of pitch and roll attitude captures of varying magnitude and command intensity. In addition, a number of simulated engine failures were executed as well. Some turbulent air layers were encountered during the flight tests hence the controller response to turbulence could be verified. Finally, the incremental controller was used during an instrument approach and was active down to an altitude of 2000 ft.

For safety reasons, the attitude captures were first executed using a conservative setup with restricted control authority and a conservative parameter set. Artificial limits on the control signals allow maximum control deflection changes of $\pm 1°$ around the trim condition. The conservative parameters are obtained by multiplying the inverse of the control effectiveness by a factor 2.

To enhance safety, situational awareness and efficiency, a strict procedure was maintained during the execution of the experiments. First the safety pilot would trim the aircraft for the desired airspeed in horizontal flight. At the same time the flight test engineer would select the desired controller configuration in the FBW computer. Conformation from both the safety pilot and flight test engineer would trigger the evaluation pilot to enable the FBW system and start the experiment. Initialization was executed with "hands-of-stick" to prevent undesirable initial control inputs.

The primary flight display was slightly modified with the addition of a marker displaying the commanded roll angle ϕ_{com}. This to enhance the situational awareness of the evaluation pilot.

2. Results

Before each flight, extensive ground testing was performed to validate proper functioning in interaction of the experimental controller with the aircraft systems. The first flight test was mainly used for familiarization due to limited experience with the test platform. Some issues were experienced due to hysteresis of the sidestick. Due to initialization problems with the actuator models, it turned out to be more effective to use measured control deflections. The FBW input-output gain K_{fbw} proofed to be smaller than estimated, resulting in a slight reduction in control effectiveness with a more conservative response as a result. As expected, the INDI control signals turned out to be noisier compared to the NDI control signals.

The response at 200 KIAS and 240 KIAS was similar albeit the latter airspeed proofed to be too close to the never-exceed-speed of the aircraft and some of the experiments had to be aborted prematurely. In the preceding experiments the airspeed was reduced to 220 KIAS. The conservative setup resulted in an overall slower response as expected. Deflection limiting did not have a perceivable effect on the pitch response as the maximum deflection changes were below the 1° limit value.

The authority of the FBW system proofed to be limited in the pitch channel with maximum pitch rates below 1°/s. No satisfactory pitch tracking could initially be achieved, with moderate pitch rate commands often resulting in large overshoots and excitation of the phugoid mode of the aircraft. The overshoot tendency was caused by the large difference between the pitch rate commanded by the pilot $\dot{\theta}_{com}$ and subsequent aircraft response. When the evaluation pilot aimed for a certain pitch attitude, command was withdrawn as soon as the aircraft reached the desired pitch attitude. However, the commanded pitch attitude θ_{com} is obtained via integration of $\dot{\theta}_{com}$ and does not take into account possible offsets between commanded and actual pitch rate. As a result, the integrated pilot rate command would exceed the desired pitch attitude causing a perceived overshoot. As no marker for θ_{com} was available on the primary flight display, the pilot had no knowledge about the commanded pitch attitude making accurate pitch attitude captures difficult to execute. Due to limited repeatability options, a successful series of pitch attitude captures could not be realized. The remainder of the discussion will therefore be limited to the lateral tracking task only.

In Figure 10 the lateral tracking response is visualized for a typical part of the flight with various roll attitude captures. Both controller types displayed favorable tracking behavior and were able to follow the imposed dynamics with small overshoot values of 1°. Notice the "jumps" in the roll command signal around 4052 s and 4070 s for the INDI controller, and around 2349 s and 2370 s for the NDI controller. At these instances the roll angle exceeded ±27° and the command module subsequently switches from RCAH to AC. The reference model ensures a smooth transition between these control laws as seen in the reference signal. AC is governed up to the roll angle limit of ±31°. Despite the higher control authority compared to the pitch channel, moderate roll commands still resulted in actuator saturation.

In Figure 11 the lateral tracking response for several roll attitude captures is visualized with PCH activated. The major difference compared to the response of the non-hedging controller is the slower response of the reference signal and the tight coupling with the aircraft response. The reference signal does not fall outside the performance envelope of the aircraft. PCH significantly reduces the saturation effect on the aileron deflections δ_a. Howhever, more noise is propagated through the control laws. The steady-state offset between command and reference/response roll angle is the result of a steady difference between the commanded and actual control deflection due to the mismatch of K_{fbw}. PCH adapts the reference model to this difference resulting in a steady error between the command and reference signal. This behavior can be avoided using actuator models instead of measured deflections.

The simulated engine failures were handled well by both the INDI and NDI controller, see Figure 12. Some oscillations were observed in the roll channel for NDI, the use of the conservative setup might have initiated this behavior. A more aggressive engine failure was simulated with the INDI controller in the loop, with an additional reversing of the differential thrust at 4550 s. The controller compensated for the asymmetric thrust in a smooth and jolt free manner. The evaluation pilot was able to perform small roll maneuvers without issues.

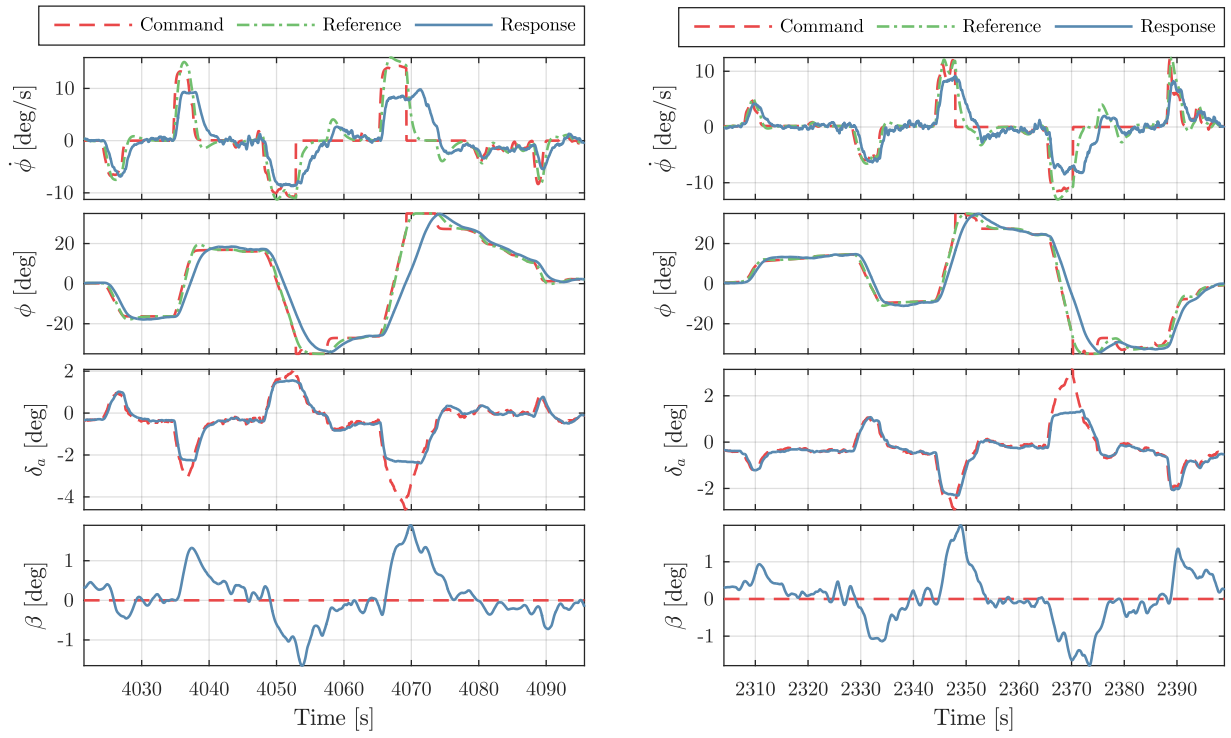

(a) INDI (nominal setup)

(b) NDI (nominal setup)

Figure 10. Lateral tracking response roll attitude captures (200 KIAS FL150)

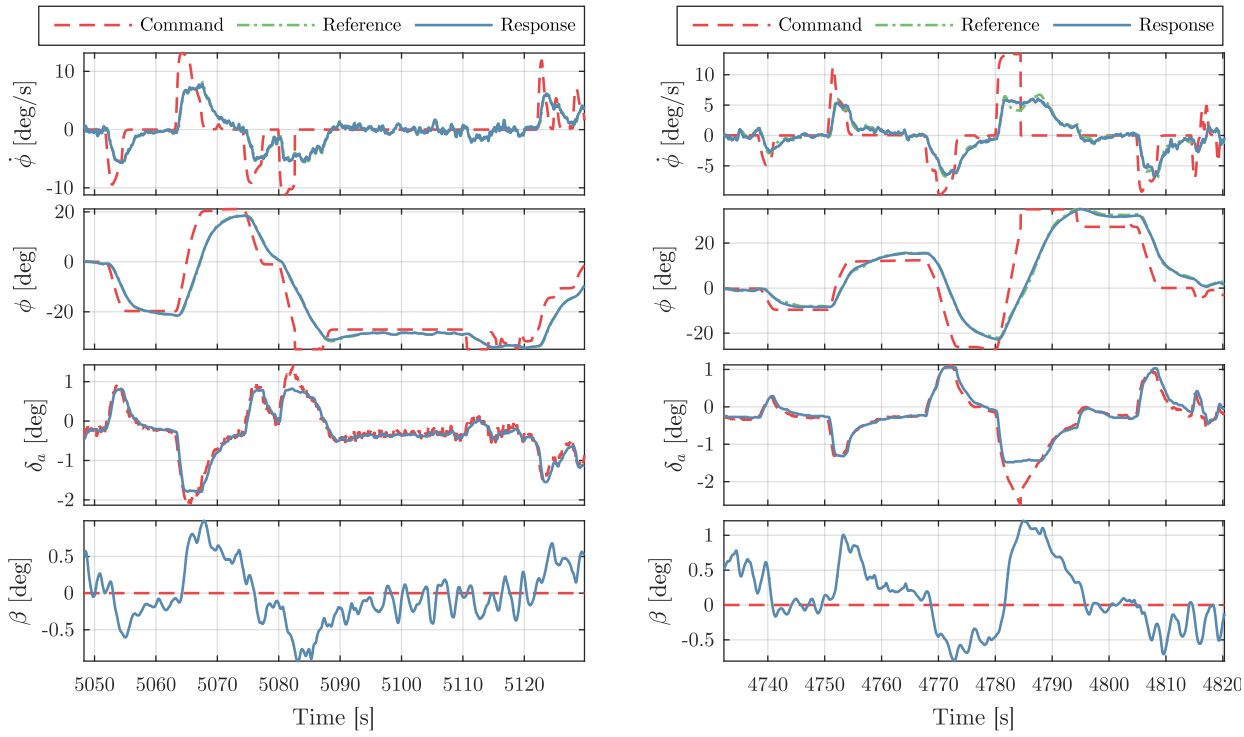

(a) INDI (nominal setup)

(b) NDI (nominal setup)

Figure 11. Lateral tracking response roll attitude captures with PCH activated (200 KIAS FL150)

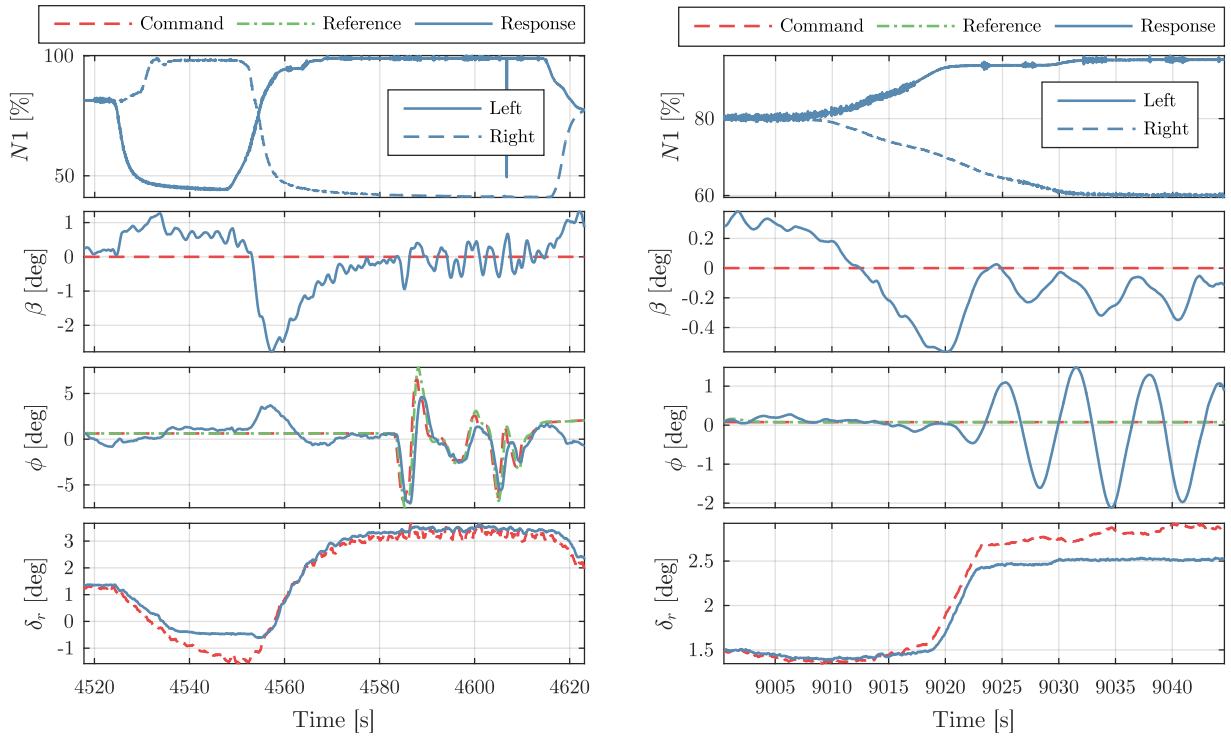

(a) INDI (nominal setup)

(b) NDI (conservative setup)

Figure 12. Lateral tracking response simulated engine failure (200 KIAS FL150)

VI. Conclusion

This paper presented the design and validation of manual attitude control functions based on Incremental Nonlinear Dynamic Inversion (INDI) for a Cessna Citation II experimental aircraft, covering control structure design, application of INDI, design optimization, robustness analyses, software implementation, ground and flight testing. For comparison, also control laws based on classical Nonlinear Dynamic Inversion (NDI) were implemented and flown.

Extensive robustness analysis revealed that INDI provides a highly robust control solution with respect to model uncertainties compared to classical NDI, even in presence of unsynchronized angular acceleration and control deflection feedback. Under the combined effect of actuators, sensors, filters, wind disturbance and model and synchronization mismatches, INDI provided a better compromise between command response, disturbance rejection and robustness compared to classical NDI.

Qualitative flight test with the INDI and NDI attitude control laws were performed on the Cessna Citation II PH-LAB, marking the first successful demonstration of INDI on a CS-25 certified aircraft. In presence of limited authority, uncertain control effectiveness and simulated engine failures, the system dynamics were canceled well by both controllers. The imposed reference dynamics were accurately tracked with nominal control effectiveness parameters, validating the simulation results.

Pseudo Control Hedging (PCH) proofed to be a valuable addition to INDI in reducing the effects of actuator saturation. To limit additional noise and uncertainties in the closed-loop system, activation of PCH only upon actuator saturation is suggested for future applications. This can for example be achieved via a simple algorithm that detects an offset between commanded and actual control deflection. For control deflection feedback, models might be preferred over measurements in certain cases as PCH adapts the reference model to any bias between commanded and actual control deflection.

A point of attention are the relatively high noise levels in the control signals of INDI. This may cause excessive wear on the actuators. Fortunately, low-noise angular acceleration measurement or estimation methods are already available in the form of angular accelerometers, linear accelerometer pairs or complimentary filters.[32]

The PH-LAB and the experimental on-board infrastructure proofed to be a reliable and efficient platform

for the testing of advanced flight control laws. For future applications it is advised that the servo motor position controller is replaced with a control law that uses the control surface deflections as feedback. This will mitigate issues with varying control effectiveness. Reducing the (electronic) torque limitations on the servo motors would also be a valuable addition to improve control authority.

Acknowledgments

The authors would like to thank the following persons from Delft University of Technology: Alexander in 't Veld, Ferdinand Postema, Hans Mulder, Menno Klaassen and Olaf Stroosma. Their support and guidance during the project is highly appreciated!

References

[1]Balas, G. J., "Flight control law design: An industry perspective," *European Journal of Control*, Vol. 9, No. 2-3, 2003, pp. 207–226.

[2]Walker, G. P. and Allen, D. A., "X-35B STOVL flight control law design and flying qualities," *Biennial International Powered Lift Conference and Exhibit*, 2002, pp. 5–7.

[3]Goupil, P., Boada-Bauxell, J., Marcos, A., Cortet, E., Kerr, M., and Costa, H., "AIRBUS efforts towards advanced real-time fault diagnosis and fault tolerant control," *IFAC Proceedings Volumes*, Vol. 47, No. 3, 2014, pp. 3471–3476.

[4]Goupil, P. and Marcos, A., "Advanced diagnosis for sustainable flight guidance and control: The European ADDSAFE project," Tech. rep., SAE technical paper, 2011.

[5]Enns, D., Bugajski, D., Hendrick, R., and Stein, G., "Dynamic inversion: an evolving methodology for flight control design," *International Journal of Control*, Vol. 59, No. 1, 1994, pp. 71–91.

[6]Lombaerts, T., Looye, G., Chu, Q., and Mulder, J., "Design and simulation of fault tolerant flight control based on a physical approach," *Aerospace Science and Technology*, Vol. 23, No. 1, 2012, pp. 151–171.

[7]Smith, P. R., "A Simplified Approach to Nonlinear Dynamic Inversion Based Flight Control," *AIAA Atmospheric Flight Mechanics Conference and Exhibit*, 1998, pp. 762–770.

[8]Smith, P. and Berry, A., "Flight test experience of a non-linear dynamic inversion control law on the VAAC Harrier," *Atmospheric Flight Mechanics Conference*, 2000, p. 3914.

[9]Bacon, B., Ostroff, A. J., and Joshi, S., "Reconfigurable NDI Controller Using Inertial Sensor Failure Detection & Isolation," *Aerospace and Electronic Systems, IEEE Transactions on*, Vol. 37, No. 4, 2001, pp. 1373–1383.

[10]Sieberling, S., Chu, Q. P., and Mulder, J. A., "Robust Flight Control Using Incremental Nonlinear Dynamic Inversion and Angular Acceleration Prediction," *Journal of Guidance, Control, and Dynamics*, Vol. 33, No. 6, 2010, pp. 1732–1742.

[11]Acquatella, P., Falkena, W., van Kampen, E.-J., and Chu, Q. P., "Robust nonlinear spacecraft attitude control using incremental nonlinear dynamic inversion," *AIAA Guidance, Navigation, and Control Conference*, 2012, pp. 1–20.

[12]Simplício, P., Pavel, M., Van Kampen, E., and Chu, Q., "An acceleration measurements-based approach for helicopter nonlinear flight control using Incremental Nonlinear Dynamic Inversion," *Control Engineering Practice*, Vol. 21, No. 8, 2013, pp. 1065–1077.

[13]Lu, P. and van Kampen, E.-J., "Active fault-tolerant control for quadrotors subjected to a complete rotor failure," *Intelligent Robots and Systems (IROS), 2015 IEEE/RSJ International Conference on*, IEEE, 2015, pp. 4698–4703.

[14]Smeur, E. J., Chu, Q., and de Croon, G. C., "Adaptive incremental nonlinear dynamic inversion for attitude control of micro air vehicles," *Journal of Guidance, Control, and Dynamics*, 2015.

[15]Vlaar, C., *Incremental Nonlinear Dynamic Inversion Flight Control: Implementation and Flight Test on a Fixed Wing UAV*, Master's thesis, Delft University of Technology, Faculty of Aerospace Engineering, 2014.

[16]van Ekeren, W., Looye, G., Kuchar, R. O., Chu, Q. P., and Van Kampen, E.-J., "Design, Implementation and Flight-Tests of Incremental Nonlinear Flight Control Methods," *2018 AIAA Guidance, Navigation, and Control Conference*, 2018, p. 0384.

[17]Zaal, P., Pool, D., Veld, A. I. t., Postema, F., Mulder, M., Paassen, M. V., and Mulder, J., "Design and Certification of a Fly-by-Wire System with Minimal Impact on the Original Flight Controls," *AIAA Guidance, Navigation, and Control Conference*, Oct 2009.

[18]Lombaerts, T. and Looye, G., "Design and flight testing of manual nonlinear flight control laws," *AIAA Guidance, Navigation, and Control Conference*, Aug 2011.

[19]Johnson, E. N. and Calise, A. J., "Pseudo-control hedging: A new method for adaptive control," *Advances in navigation guidance and control technology workshop*, 2000, pp. 1–2.

[20]Looye, G., Willemsen, D., Bauschar, J., and Moennich, W., "Flight testing robust autoland control laws," *AIAA Guidance, Navigation, and Control Conference and Exhibit*, Jun 2001.

[21]Lombaerts, T. and Looye, G., "Design and flight testing of nonlinear autoflight control laws," *AIAA Guidance, Navigation, and Control Conference*, 2012, p. 4982.

[22]Lombaerts, T. and Looye, G., "Design and Flight Testing of Nonlinear Autoflight Control Laws Incorporating Direct Lift Control," *Advances in Aerospace Guidance, Navigation and Control*, 2013, pp. 549568.

[23]van Paassen, M. M., Stroosma, O., and Delatour, J., "DUECA - Data-Driven Activation in Distributed Real-Time Computation," *Proceedings of the AIAA Modeling and Simulation Technologies Conference and Exhibit, Denver (CO)*, No. AIAA-2000-4503, Aug. 2000.

[24]Mulder, M., Lubbers, B., Zaal, P., Paassen, M. V., and Mulder, J., "Aerodynamic Hinge Moment Coefficient Estimation Using Automatic Fly-by-Wire Control Inputs," *AIAA Modeling and Simulation Technologies Conference*, Oct 2009.

[25]van't Veld, R., Van Kampen, E.-J., and Chu, Q. P., "Stability and Robustness Analysis and Improvements for Incremental Nonlinear Dynamic Inversion Control," *2018 AIAA Guidance, Navigation, and Control Conference*, 2018, p. 1127.

[26]Linden, C. A. A. M. v. d., *DASMAT-Delft University aircraft simulation model and analysis tool: a Matlab/Simulink environment for flight dynamics and control analysis*, Delft University Press, 1998.

[27]van den Hoek, M. A., de Visser, C. C., and Pool, D. M., "Identification of a Cessna Citation II Model Based on Flight Test Data," *Proceedings of the 4th CEAS Specialist Conference on Guidance, Navigation & Control, Warsaw, Poland*, 2017.

[28]de Visser, C. C., *Global Nonlinear Model Identification with Multivariate Splines*, Phd thesis, Delft University of Technology, Faculty of Aerospace Engineering, June 2011.

[29]Looye, G. and Joos, H.-D., "Design of robust dynamic inversion control laws using multi-objective optimization," *Proceedings of the AIAA Guidance, Navigation and Control Conference*, 2001.

[30]Joos, H.-D., "A methodology for multi-objective design assessment and flight control synthesis tuning," *Aerospace Science and Technology*, Vol. 3, No. 3, 1999, pp. 161–176.

[31]Bellmann, T., Heindl, J., Hellerer, M., Kuchar, R., Sharma, K., and Hirzinger, G., "The dlr robot motion simulator part i: Design and setup," *Robotics and Automation (ICRA), 2011 IEEE International Conference on*, IEEE, 2011, pp. 4694–4701.

[32]Grondman, F., *Dynamic Inversion Flight Control Law Design for Fixed-Wing Aircraft: Design and Flight Testing of Incremental Nonlinear Dynamic Inversion based Control Laws for a Passenger Aicraft*, Master's thesis, Delft University of Technology, Faculty of Aerospace Engineering, 2018.